Unraveling the stereochemical and dynamic aspects of the catalytic site of bacterial peptidyl-tRNA hydrolase

ASHISH KABRA,[1,4] SALMAN SHAHID,[1,2,4] RAVI KANT PAL,[3] RAHUL YADAV,[1]
S.V.S. RAMA KRISHNA PULAVARTI,[1] ANUPAM JAIN,[1] SARITA TRIPATHI,[1] and ASHISH ARORA[1,2]

[1]Molecular and Structural Biology Division, CSIR-Central Drug Research Institute, Lucknow 226031, India
[2]Academy of Scientific and Innovative Research, New Delhi 110025, India
[3]X-ray Crystallography Facility, National Institute of Immunology, New Delhi 110067, India

ABSTRACT

Bacterial peptidyl-tRNA hydrolase (Pth; EC 3.1.1.29) hydrolyzes the peptidyl-tRNAs accumulated in the cytoplasm and thereby prevents cell death by alleviating tRNA starvation. X-ray and NMR studies of *Vibrio cholerae* Pth (VcPth) and mutants of its key residues involved in catalysis show that the activity and selectivity of the protein depends on the stereochemistry and dynamics of residues H24, D97, N118, and N14. D97-H24 interaction is critical for activity because it increases the nucleophilicity of H24. The N118 and N14 have orthogonally competing interactions with H24, both of which reduce the nucleophilicity of H24 and are likely to be offset by positioning of a peptidyl-tRNA substrate. The region proximal to H24 and the lid region exhibit slow motions that may assist in accommodating the substrate. Helix α3 exhibits a slow wobble with intermediate time scale motions of its N-cap residue N118, which may work as a flypaper to position the scissile ester bond of the substrate. Overall, the dynamics of interactions between the side chains of N14, H24, D97, and N118, control the catalysis of substrate by this enzyme.

Keywords: peptidyl-tRNA hydrolase; catalytic mechanism; protein structure; relaxation dynamics; MD simulations; thermostability

INTRODUCTION

The process of protein translation is the target of several clinically used antimicrobial drugs. This process is aborted prematurely in 10% of cases due to ribosome stalling, and also because of minigenes expression and effect of macrolide antibiotics (Menninger 1976; Caplan and Menninger et al. 1979; Heurgue-Hamard et al. 1998; Karimi et al. 1998; Cruz-Vera et al. 2004). The stalling and subsequent disruption of the ribosome leads to accumulation of peptidyl-tRNA in the cytosol. This accumulation is toxic to the cells and also creates scarcity of free tRNA for further protein synthesis (Menninger 1979). This condition is salvaged by an enzyme, peptidyl-tRNA hydrolase (Pth), which cleaves the ester linkage between the C-terminal carboxyl group of the peptide and the 2′- or 3′-hydroxyl of the ribose at the 3′ end of tRNA, thus releasing free peptides and tRNA for reuse in protein synthesis (Atherly 1978; Das and Varshney 2006). Pth activity has been demonstrated to be essential for the viability of *Bacillus subtilis*, *Escherichia coli*, and *Mycobacterium tuberculosis* (Cruz-vera et al. 2000; Menez et al. 2002; Bal et al. 2007). Therefore, bacterial Pths are a strong candidate for the development of antibacterial agents. X-ray crystal structures of Pth from *Escherichia coli*, *Mycobacterium tuberculosis*, *Mycobacterium smegmatis*, *Francisella tularensis*, *Pseudomonas aeruginosa*, *Acinetobacter baumannii*, *Salmonella typhimurium*, *Streptococcus pyogenes*, and *Staphylococcus aureus* have been determined (Schmitt et al. 1997; Bonin et al. 2002; Selvaraj et al. 2007; Clarke et al. 2011; Hughes et al. 2012; Kumar et al. 2012; Kaushik et al. 2013; Singh et al. 2014a,b; Vandavasi et al. 2014). On the other hand, the two NMR solution structures that have been solved are of *Mycobacterium tuberculosis* Pth and *Mycobacterium smegmatis* Pth (Pulavarti et al. 2008; Kabra et al. 2016). X-ray characterization of Pth with bound bases, substrate mimics, and acceptor-TψC fragments of tRNA have also been reported (Ito et al. 2012; Kaushik et al. 2013; Singh et al. 2014a,b). NMR-based chemical shift perturbation studies have been carried out for EcPth in the presence of a minimal substrate analog (Giorgi et al. 2011b), and uncharged fragments of tRNA (Giorgi et al. 2011a). In the case of Pth enzymes, the

[4]**These authors contributed equally to this work.**
Corresponding author: ashish_arora@cdri.res.in
Article is online at http://www.rnajournal.org/cgi/doi/10.1261/rna.057620.116.

catalytic site resides in a crevice on the surface of the protein. The base of the crevice is defined by the N-terminal ends of helices α2 and α3, and the segment G111-H117 (all numbering is with reference to the VcPth sequence), which has been termed as the "base loop." The face of the crevice opposite to the base loop is defined by the segment L99-V105, termed as the "gate loop." The crevice is covered from the top by a mobile loop-helix element formed by segment H142-L154, termed as the "lid" region (Fig. 1). The catalytic site is defined by residues N14, H24 (catalytic base), N72, D97, and N118. On one end of the H24 is the peptide binding region defined by residues N14, N72, and N118 (Schmitt et al. 1997). N14 is the residue implicated for substrate specificity, i.e., peptidyl-tRNA substrate selection and discrimination from amino-acyl-tRNA (Giorgi et al. 2011b). On the opposite end is the 5′-phosphate clamping region defined by basic residues K107, K109, and R137 (Schmitt et al. 1997; Fromant et al. 1999; Ito et al. 2012). In between the catalytic base H24 and the phosphate binding region, an open or closed state of a "gate" between the peptidyl and the tRNA region has been proposed to be contributed by positioning of the opposing gate loop and the base loop (Selvaraj et al. 2007). Docking simulations based on ambiguous restraints derived from an NMR chemical shift perturbation study involving EcPth and a minimal substrate mimic, 3-(L-[*N*,*N*-diacetyl-lysinyl) amino-3-deoxyadenosine, has shown that the mimic's peptide moiety interacts with residues N10, N68, and N114 of EcPth, with the side-chain NH_2 group of N10 holding the main-chain carbonyl of the penultimate C-terminal amino acid residue (Giorgi et al. 2011b). A similar NMR-based docking simulations study with a mimic RNA helix containing the acceptor and TψC stems of $tRNA^{His}$ with EcPth has found that the catalytic site, lid loop, gate loop, base loop, the phosphate clamping basic residues, and the C-terminal helix are important for Pth-tRNA interactions (Giorgi et al. 2011a).

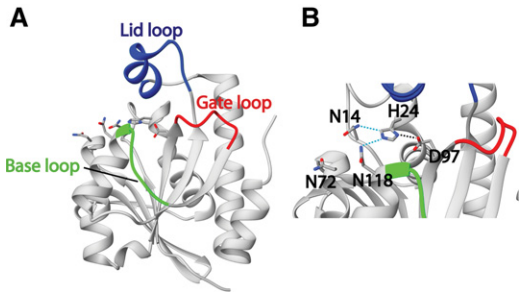

FIGURE 1. Structural depiction of VcPth crystal structure (PDB ID: 4ZXP) showing important loop regions and catalytic site residues. (*A*) Cartoon representation of VcPth showing base loop in green color, gate loop in red color, and lid loop in blue color. Catalytic site residues (N14, H24, N72, D97, and N118) are shown as sticks. (*B*) Enlarged representation of the catalytic site showing important catalytic residues, which are labeled. Black dashes indicate a conserved hydrogen bond between H24 and D97. Cyan dashes represent the possible interactions between N14-H24 and H24-N118.

In the Pth-CCA-acceptor-TψC crystal structure, no interaction is seen between Pth and the CCA end. However, the 3′-adenine of the acceptor arm has been docked in a cavity. In the docked model, it forms hydrogen bonds with G111 and has van der Waal's contacts with L95 and V149 (Ito et al. 2012). The minor groove of the TψC arm has been shown to interact with helix α6 (Ito et al. 2012), while the acceptor-CCA end has been proposed to be clamped by K146. Hames et al. (2013) have studied Pth-peptidyl-tRNA complex with SANS and have developed a low resolution model in which, unlike the Pth-CCA-acceptor-TψC crystal structure, there is an end to end interaction and almost no overlap between the Pth and tRNA regions. This has been suggested to reflect a later step in the reaction, i.e., a pre-product dissociation complex.

Extensive mutational studies have been performed to delineate the roles of residues corresponding to N14, H24, N72, D97, and N118, in enzyme catalysis. Schmitt et al. (1997) have reported a K_m of 6.0 μM for wt-EcPth, and K_m values of 6.6 μM and 10 μM for its N10A and D93A mutants, respectively. Fromant et al. (1999) have reported K_m values of 12.5 μM and 3.9 μM, for the EcPth N68A and N114A mutants, respectively. Fromant and coworkers concluded that the N10A, N68A, D93A, and N114A mutations did not significantly contribute to the stability of the enzyme–substrate complex. Further, they also noted that mutations of N10, N68, N114, and D93 were associated with reduction of the k_{cat} parameter by two orders of magnitude. In a separate study, Goodall et al. (2004) found a K_m of 5.5 μM for the wt-EcPth, while the K_m for its D93N and N10D mutants was found to be 3.8 μM and 7.9 μM, respectively. For the mutants, a decrease in k_{cat} by two orders of magnitude was observed. In all these studies, a mutation of H20 caused a complete loss of enzyme activity such that the k_{cat} and K_m parameters could not be determined. However, Goodall et al. (2004) were also able to show from transient kinetics experiments that the H20N mutant of EcPth retained the ability to bind to the substrate. Based on mutagenesis, enzyme activity, and chemical modification studies, H20 has been shown to be the critical base necessary for the catalysis. Further, Giorgi et al. 2011b have reported that diacetyl-Lys-$tRNA^{lys}$ was hydrolyzed by wt-EcPth 360-fold more efficiently than Lys-$tRNA^{lys}$. In contrast, the fold difference for N10D mutant was found to be 0.8. Therefore, they proposed that the N10 is the residue responsible for discrimination between the N-protected amino-acyl-tRNA and free amino-acyl-tRNA. Further, based on structural studies and model building, it was suggested that the N10 side-chain amide binds to the carbonyl of the first peptide bond from the C-terminal amino acid.

The plausible general mechanism of hydrolysis is depicted in Figure 2 (Goodall et al. 2004; Ito et al. 2012). A conserved hydrogen bond between D97 and H24 stabilizes the anionic form of the latter, which then abstracts a proton from a proximal water molecule. The resulting hydroxyl nucleophilically

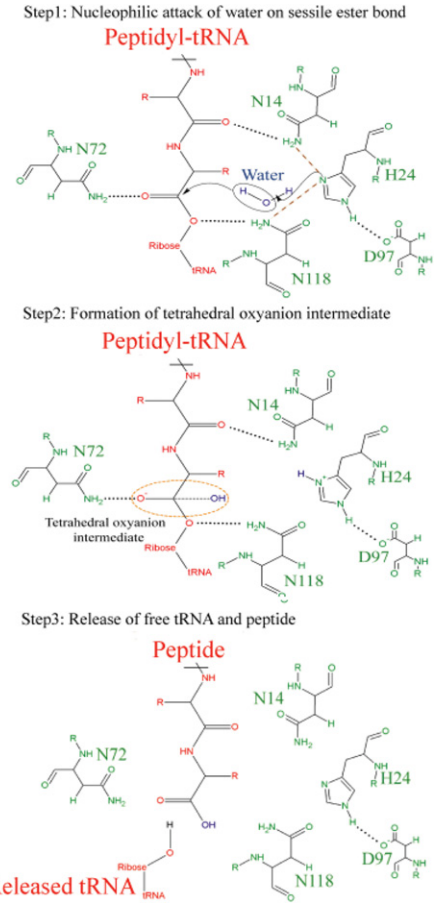

FIGURE 2. Schematic representation of the three step (nucleophilic attack of hydroxyl ion, formation of oxyanion intermediate, and release of free tRNA and peptide moieties) catalysis reaction of bacterial Pths. Important residues of Pth enzyme (numbered according to VcPth) are shown in green and substrate peptidyl-tRNA is shown in red. The H-bonds are shown in black dashes. The possible interactions between N14-H24 and H24-N118 are shown in brown dashes in step 1.

attacks the carbon of the scissile ester and the intermediate tetrahedral state is stabilized by hydrogen bonding to the side chains of N72 and N118 (Goodall et al. 2004; Giorgi et al. 2011b; Ito et al. 2012). The decomposition of the intermediate completes the hydrolysis reaction. However, in the absence of structures of the enzyme bound to substrate or any of the reaction intermediates, the structural understanding of the mechanism of enzyme action has been limited to defining the conformational dynamics (plasticity) of the base loop, gate loop, and lid loop. Further, the plasticity has only been derived, up to now, from the comparison of crystal structures of Pth proteins from various species.

Initally, based on the comparison of crystal structures of EcPth and MtPth, it was proposed that the opening of the gate was correlated to orientational changes resulting from the binding of peptide at the peptidyl-site of Pth. As per this hypothesis, the gate and lid distances were inversely correlated, i.e., opening of the gate was correlated to the closing of the lid region (Selvaraj et al. 2007). However, such a correlation was not found in the crystal structures determined subsequently (Bonin et al. 2002; Hughes et al. 2012; Kaushik et al. 2013; Singh et al. 2014a,b; Vandavasi et al. 2014). Therefore, this hypothesis still needs a sound experimental basis. In spite of the availability of many structures, and even though critical residues involved in catalysis are highly conserved, the stereochemistry and dynamics of the catalytic site and determinants of substrate specificity are not clearly understood.

In order to improve this understanding, we have selected a bacterial Pth from *V. cholerae*, and have determined its X-ray crystal and NMR solution structures. We have performed mutational analysis of the residues that are highly conserved and have also been shown to be essential for the enzyme activity, i.e., N14, H24, N72, D97, and N118 (Fromant et al. 1999; Goodall et al. 2004). The crystal structures of the N14D, H24N, D97N, and N118D mutants have been determined. In order to have a physiological solution state understanding, backbone chemical shift assignments have been done for N14D, H24N, N72D, and N118D mutants, and the conformational perturbations caused by the mutations, in solution, have been monitored by mapping the chemical shift perturbations (CSPs), with reference to the wild-type protein. Backbone relaxation experiments using NMR and MD simulation study for wt-VcPth and its mutants were also performed to analyze the changes in local flexibility of the protein. Further, thermal stability of wt-VcPth and the mutants was analyzed using differential scanning calorimetry (DSC).

RESULTS

The ensemble of 10 superimposed backbone traces, representing the solution structure of wt-VcPth (PDB ID: 2MJL), is shown in Figure 3A, and the cartoon representation of the structure having the lowest energy is shown in Figure 3B. The NMR structure statistics are summarized in Supplemental Table S1. The crystal structure of wt-VcPth was solved at 1.63 Å resolution (PDB ID: 4ZXP). Based on Matthew's calculation (2.38 $Å^3$ Da^{-1}, 48.43% solvent content), it has two molecules in the asymmetric unit, which form an apparent dimer, and is shown in Figure 3C. The interactions between two chains of the asymmetric unit are shown in Supplemental Figure S1. The final model consisted of 393 residues along with one citrate ion and 331 water molecules. Refinement and structure data are summarized in Supplemental Table S2. The structure is composed of a twisted central mixed β-sheet consisting of seven β-strands. This central core has two antiparallel strands β2 and β3 followed by four parallel strands β4, β1, β5, and β7, and one antiparallel strand β6. Six α-helices cover the central β-sheet core from various directions. Helices α2 and α3 cover the core from the peptidyl side while the C-terminal helices α5 and α6 are on the other side. Helix α1 covers the central core from the third side whereas helix α4 is part of the most

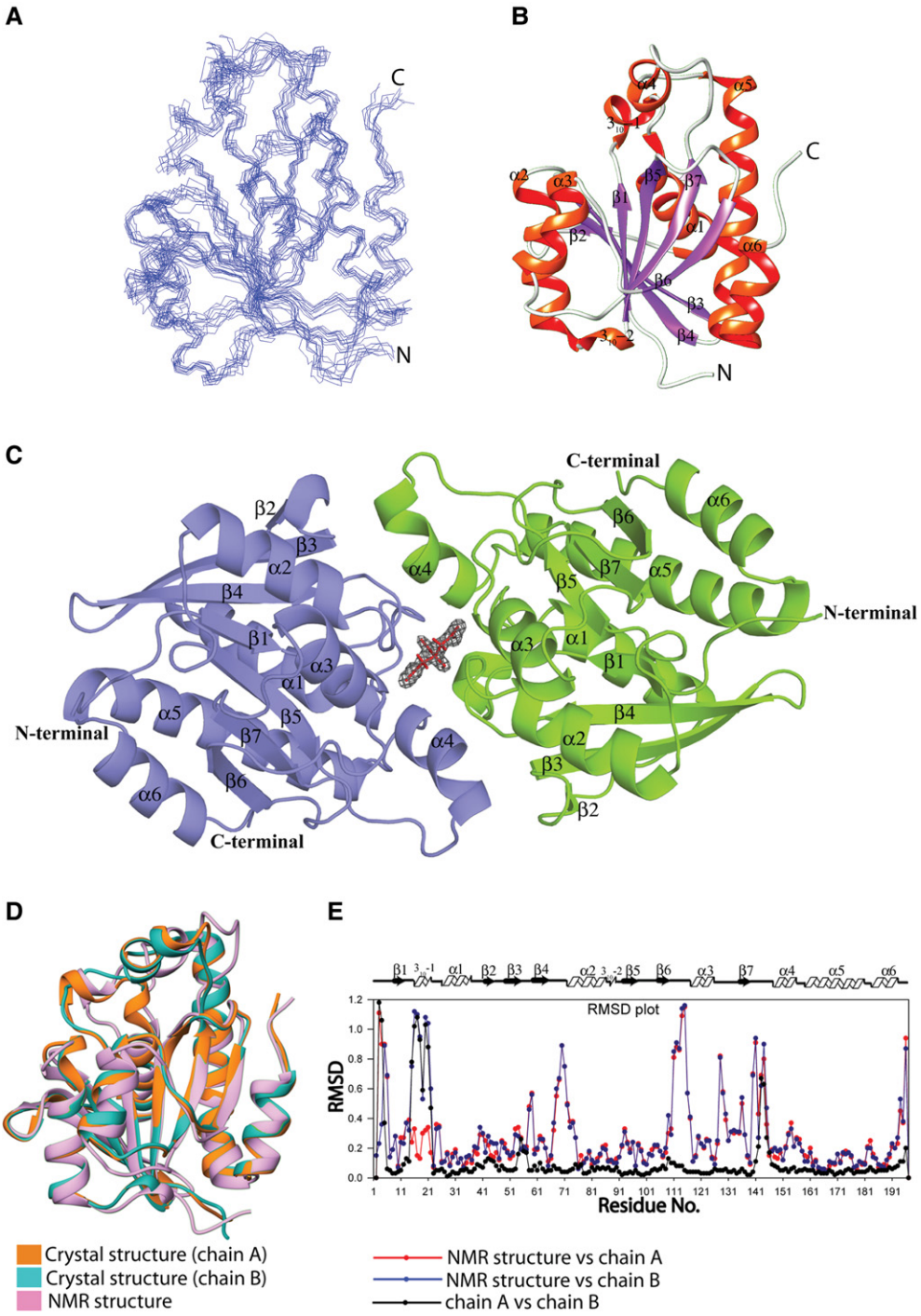

FIGURE 3. Solution structure and crystal structure of *Vibrio cholerae* peptidyl-tRNA hydrolase (PDB IDs: 2MJL and 4ZXP, respectively): (*A*) Superimposition of backbone traces from the final ensemble of 10 solution structures of VcPth with lowest target functions; (*B*) Cartoon representation of lowest energy structure of VcPth solution structure (2MJL). N-terminal, C-terminal, and the individual α-helices and β-strands are labeled; (*C*) Cartoon representation of crystal structure of VcPth (4ZXP) showing two protein molecules in the crystallographic unit cell colored green and blue for chains *A* and *B*, respectively. Citrate molecule is shown at the interface by sticks having $2F_o$-F_c electron densities contoured at 2σ; (*D*) Superimposition of VcPth solution structure with the chain *A* and chain *B* of VcPth crystal structure; (*E*) Residue wise RMSD plot showing RMSDs among the VcPth solution structure, A chain, and B chain of the VcPth crystal structure.

flexible segment of the molecule and is situated over a crevice on the surface of the protein. Although the solution structure and both the chains of crystal structure are very similar, the lengths of some of the secondary structural elements differ slightly. The secondary structural elements for the solution and crystal structures are given in Supplemental Table

S3. The two polypeptide chains in the asymmetric unit of the crystal structure show a root mean square deviation (RMSD) of 0.9 Å for 196 Cα atoms upon superimposition. With the solution structure, chain A and chain B display Cα rmsds of 1.9 Å and 2.1 Å, respectively, over residues 2–197. The overlap of the NMR lowest energy structure with both chains of crystal structure is shown in Figure 3D, and RMSD as a function of residue number among these structures is plotted in Figure 3E.

A citrate ion is trapped at the interface of chain A and chain B. The citrate ion is within 4.2 Å distance of residues N14, P15, Y19, H24, F70, M71, N72, N118, G119, and L154 of chain A, and the corresponding residues of chain B, except for Y19. The citrate ion forms hydrogen bonds with N14, H24, M71, and N118 of each monomer. The citrate ion is involved in one salt bridge, eight hydrogen bonds, and two unconventional hydrogen bonds, as shown in Supplemental Figure S2. Two anion–π interactions between the citrate and VcPth crystal structure are shown in Supplemental Figure S2. The intermolecular hydrogen bond distances between citrate and protein residues are given in Supplemental Table S4.

For comparison, we have crystallized wt-VcPth under solvent conditions that lacked citrate. The structure of wt-VcPth from such crystals could be determined at 1.75 Å resolution in the space group $C222_1$. In this structure (PDB ID: 5VGZ), there is only one molecule in the asymmetric unit. Analysis of this structure shows that there is only a very small difference in the orientation of the side chains in the absence or the presence of citrate.

In solution, the interaction of citrates with wt-VcPth was monitored by NMR spectroscopy, by comparison of assigned NMR peak positions in the HSQC spectra of wt-VcPth in the absence and presence of 10-fold molar excess of citrate. The residue-specific chemical shift perturbations caused by citrates are shown in Supplemental Figure S2.

Structural analysis of VcPth mutants

Replacement of conserved asparagines (N10, N68, and N114) in EcPth causes significant loss in activity of *E. coli* Pth with the reduction of k_{cat} by two orders of magnitude, while the replacement of conserved catalytic histidine (H20) of *E. coli* causes complete loss of activity (Fromant et al. 1999). Based on these previous enzyme activity studies of *E. coli* Pth, we have created active site mutants of VcPth (N14D, H24N, N72D, D97N, and N118D) and mapped the structural changes by determining the crystal structures of N14D, H24N, D97N, and N118D mutants. Crystal structures of mutants show two molecules in the asymmetric unit and similar overall fold as the wt-VcPth crystal structure described above. The refinement and structure data for these mutant crystal structures are summarized with the wt-VcPth crystal structure in Supplemental Table S2. For all of the mutants, the better defined structures of the A-chains have been utilized for comparison with the wt-VcPth structure. One common difference with respect to the structure of wt-VcPth for all of the mutants is the absence of trapped citrate at the interface of the apparent dimer in all of the mutant crystal structures. NMR backbone assignments were made for N14D, H24N, N72D, and N118D mutants. Assignments could not be made for the D97N mutant, as it tended to precipitate under NMR buffer conditions. Overlays of the ^{1}H-^{15}N HSQC spectra of the wt-VcPth and different mutants (N14D, H24N, N72D, and N118D) are summarized in Figure 4. The residue wise plots for chemical shift perturbations for different mutants are shown in Supplemental Figure S3, and these CSPs mapped on the VcPth solution structure are shown in Supplemental Figure S4. Based on the magnitude, the CSPs have been categorized as very strong (range 1.2–0.8), strong (range 0.8–0.5), moderate (range 0.5–0.25), and low (range 0.25–0.1).

N14D mutant

With reference to assignments made for wt-VcPth, backbone amide resonances for D14 and D147 could not be assigned for the N14D mutant. The observed CSPs were mainly clustered in two regions: loop before 3_{10}-1 helix-to-helix α1 (A13-A28) and loop before helix α2 to helix α2 (T68-G75), as shown in Figure 4A. Beside these clustered regions, some residues of helix α3 (G119-L120) and lid loop region (G144 and V153) also showed moderate-to-high CSPs, while E32, H96, L138-G139, and G155 showed low CSPs. The N14D crystal structure showed that the side chain of D14 moves away from M71 after the mutation, which leads to loss of the conserved hydrogen bond between OD1 of N14 and N of M71. The loss of this hydrogen bond was apparent in the solution state and was indicated by very high CSP observed for the M71 NH cross peak in the HSQC spectrum. At the same time, the reciprocatory hydrogen bonding between N14 and N25, which is observed in the wt-VcPth, is conserved in the N14D mutant.

H24N mutant

The H24N crystal structure showed that the amide group of N24 partially occupies the site of the original histidine ring. The salt bridge between H24 and D97, which is conserved in all other canonical Pth structures, is lost in the H24N mutant structure of VcPth. However, N24 forms a hydrogen bond with D97, and a new hydrogen bond is also formed between N14 and N24. Hydrophobic interactions of H24 with M71 and V153 are lost upon H24N mutation. With reference to the wt-VcPth assignments, the NMR backbone resonance for R23 could not be assigned, while the peak for N118 could be assigned in the HSQC spectrum of the H24N mutant. High CSPs for this mutant were mainly clustered in two regions: helix α1 (A28-E32) and the loop before helix α2 (T68-L73), as shown in Figure 4B. Beside these clustered regions, residues N14, D97, and L120 showed moderate to high

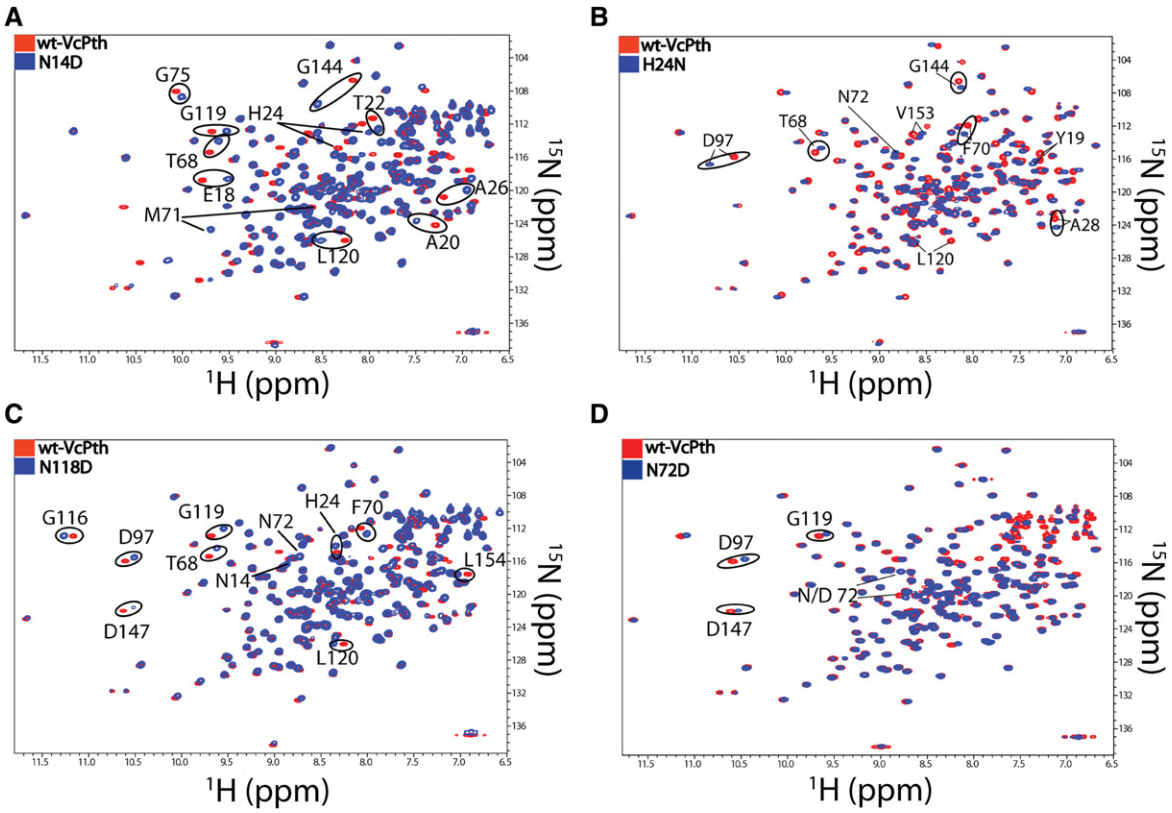

FIGURE 4. Overlapped ^{1}H-^{15}N HSQC spectra of wt-VcPth with (*A*) N14D mutant, (*B*) H24N mutant, (*C*) N118D mutant, and (*D*) N72D mutant. Red peaks represent the wt-VcPth and blue peaks represent the corresponding mutant. Some residues, which show significant CSPs, are labeled.

CSPs, while A13, Y19, N24, E98, T123 and some lid loop residues (G144, Y152, and V153) showed low CSPs.

N118D mutant

The N118D crystal structure showed change in the side-chain orientation of D118, which results in the formation of a new hydrogen bond between NE2 of H24 and OD1 of D118 after the mutation. The orientations of the D97, H24, and D118 side chains, including the D97-H24 and H24-D118 hydrogen bonds, are similar to those found between corresponding residues in the crystal structures of MtPth and MsPth (Selvaraj et al. 2007; Kumar et al. 2012). However, such relative positioning of these three side chains has not been observed in the crystal structures of most of the other bacterial Pth proteins. CSPs for this mutant were mainly clustered in two regions: loop before helix α2 (T68-L73); and helix α3 region (G116-D122), as shown in Figure 4C. Beside these two clustered regions, I6, N14, H24, D97, N129, and two residues of the lid loop region (D147 and L154) also showed low CSPs. An interesting feature of the backbone assignments for N118D is the appearance of the amide cross peak for D118. The appearance of the D118 peak is presumably due to the strong electrostatic interaction between H24 and D118, which results in a slow conformational exchange of D118 in comparison to the intermediate exchange of N118 in wt-VcPth.

D97N mutant

In the D97N crystal structure, the catalytically important hydrogen bond between D97 and H24 is lost after the mutation and a new H-bond is formed between H24 and N118. Backbone assignments were not carried out for the D97N mutant due to poor solubility of this mutant in NMR buffer conditions.

N72D mutant

For the N72D mutant, crystal structure could not be determined under similar conditions but NMR backbone assignments could be achieved. In the N72D mutant, the perturbations were found to be much less in comparison to other mutants. Residues A13, N/D72-L73, D97, G119, N129, and D147 showed low to moderate CSPs, as shown in Figure 4D. The interesting result was the appearance of N118 amide NH cross peak in the HSQC spectrum of the N72D mutant. The appearance of N118 in the N72D mutant shows a possible interaction between N72 and N118 in wt-VcPth. However, the crystal structure and NMR structure of wt-VcPth do not show this interaction.

Overall, the CSP analysis of mutants shows that the perturbation amplitude was highest for the N14D mutant in comparison to the H24N, N72D, and N118D mutants. Interestingly, the former mutation did not affect the

dynamics of N118, while the latter three mutations changed the rates of chemical exchange for the amide NH vector of residue 118. The CSP analysis also shows that the regions involving residues N14, H24, N72, D97, N118, and V153 are either directly or indirectly connected to each other through a network of interactions.

Backbone dynamics of VcPth and its mutants

The residue-specific R_1, R_2, and $\{^1H\}$-^{15}N NOE values obtained for wt-VcPth, H24N, and N118D mutants at 700 MHz are shown in Supplemental Table S5 and Supplemental Figure S5. The backbone relaxation rates of 139 out of 187 nonproline residues were considered for calculation. The average values of relaxation parameters for these residues are $R_1 = 0.93S^{-1}$, $R_2 = 19.28S^{-1}$, and $\{^1H\}$-^{15}N NOE = 0.78. Based on the R_2/R_1 ratios (Blake-Hall et al. 2004), the region proximal to the catalytic base H24, some residues of helix α2 and α3, and the C-terminal helical hairpin, are expected to exhibit motions on the slow time scale. On the other hand, the fast time scale motion is exhibited by the N-terminal region, C-terminal region, N58 of β3-β4 turn, N72 of helix α2, and lid region (H145 and D147). Moreover, the basic "flap" residue in the loop of the lid region K146 and N118 for wt-VcPth could not be observed in the HSQC spectrum.

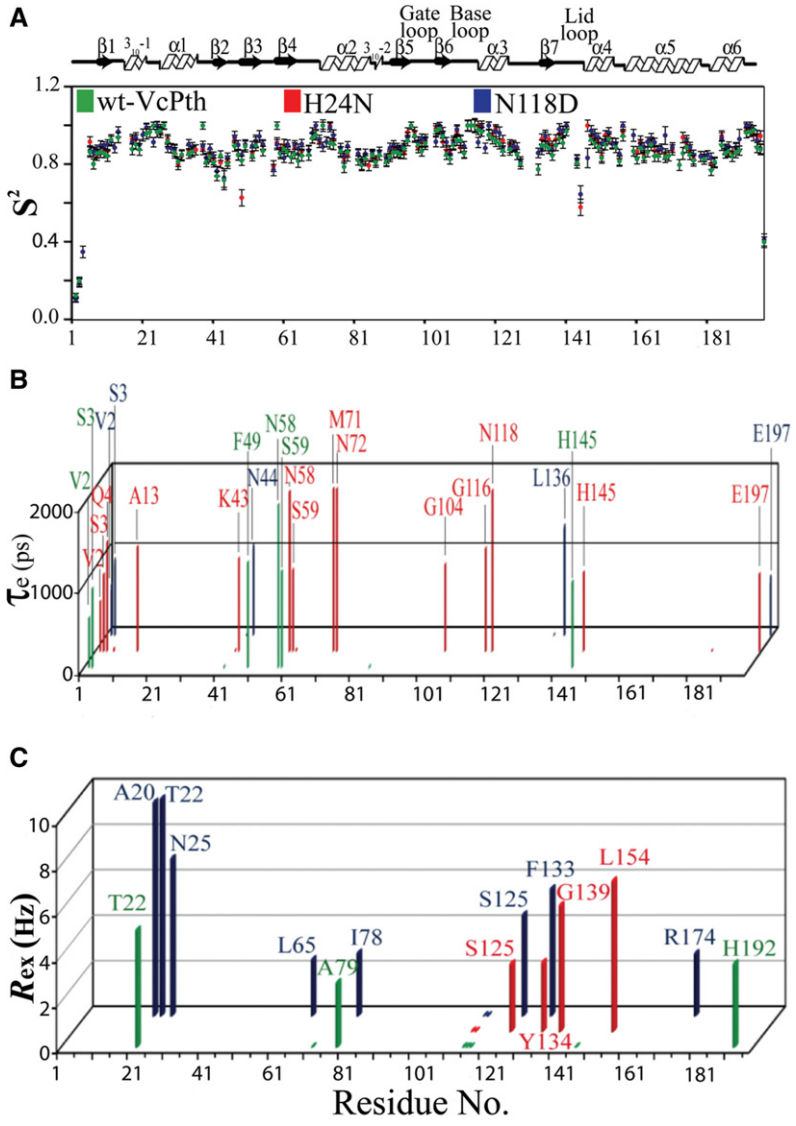

FIGURE 5. Model-free analysis of wt-VcPth (green), H24N mutant (red), and N118D mutant (blue). (*A*) Generalized order parameter (S^2), (*B*) the effective correlation time (τ_e), and (*C*) the chemical exchange parameter (R_{ex}).

An NMR relaxation study of the H24N mutant showed that the global motional mode remained similar to that of the wt-VcPth. Change in local motion was observed in the vicinity of the N24 residue, upon mutation. Further, based on the comparison of average R_2/R_1 ratios, the overall flexibility of the H24N mutant was found to be slightly increased in comparison to the wt-VcPth, as shown in Supplemental Figure S5. In the case of the N118D mutant, the relaxation parameter profiles were very similar to the wt-VcPth, indicating no change in global motional mode. For further insight, the ^{15}N relaxation parameters for wt-VcPth and mutants were analyzed by model-free formalism in order to derive the residue-specific model-free parameters S^2, τ_e, and R_{ex}. The model-free parameters for these three proteins are shown in Figure 5. Model-free analysis confirms that for wt-VcPth, the regions involving residues T22, A79, G115-H117, D147, and H192 show motions on the slow time scale that involve an R_{ex} term. On the other hand, N-terminal and the residues L42, F49, N58, S59, Y85, and H145 displayed fast time scale motions involving τ_e term for internal motions. For the H24N mutant, increased flexibility (fast time scale motions) of the regions involving residues, A13, helix α2 (M71 and N72), and the tip of helix α3 (G116 and N118) was observed in addition to the regions described for wt-VcPth. On the other hand, slow time scale motion was not observed in the vicinity of the mutated residue (N24). In contrast, slow motion was observed for the hinge residues G139 and L154 for the H24N mutant of VcPth. For the N118D mutant, more pronounced slow motions were observed in the vicinity of H24 in comparison to wt-VcPth. The possible changes for the N118D mutant in the region near N14 could not be monitored due to spectral

overlap of the A13 amide peak for this mutant. Interestingly, N118 and D118 could be assigned in the HSQC spectra of H24N and N118D mutants, respectively. Overall, the dynamics analysis indicates that the region next to the catalytic histidine (H24) and the hinge region (G139 and V153) of the lid loop exhibit slow motion fluctuations. These fluctuations may be coupled to each other in wt-VcPth through the H24-V153 interactions. Together, these motions may be perceived to help the proper accommodation of the substrate. The C-terminal helices, α5 and α6, show less wobble for all these three proteins in comparison to MtPth (Pulavarti et al. 2008). More precise characterization of molecular rotational correlation time (τ_m) and chemical exchange (R_{ex}) can be obtained from data acquired at multiple static magnetic fields. Further, for internal motions in the nanosecond range, the order parameters (S^2) and correlation times (τ_e) can be obtained from such data sets using the extended model-free formalism (Liang et al. 2010).

MD simulations of VcPth and its mutants

Protein dynamics were also analyzed by using in silico MD simulations. Residue wise RMSF values were calculated for wt-VcPth during the simulation for 2–10 ns and are plotted in Figure 6. MD simulation results for wt-VcPth are qualitatively comparable to the fast relaxation events characterized by NMR relaxation measurements, as indicated by higher RMSF values for the N-terminal region, C-terminal region, lid loop, base loop, and the loop between helixes α5 and α6. The similarity between the NMR relaxation rates and MD simulations also extends to the gate loop for which both these procedures indicate lower flexibility in comparison to the rest of the protein. The higher flexibility of base loop residues and lid loop residues may contribute to the changes in width of the substrate binding crevice, and the fluctuation of the gate distance, both of which have been suggested to be important for the substrate binding. MD simulations of the mutants confirm the observation made from NMR studies that the general global dynamics characteristics were retained upon various mutations. However, increased flexibility near the N14 residue is observed in all these mutants in comparison to wt-VcPth. Specifically, for the H24N mutant, higher flexibility is observed for the region close to N14 and α2. On the other hand, for the N118D mutant, decreased flexibility of the base loop is observed, which supports the newly formed strong electrostatic interaction between H24 and D118.

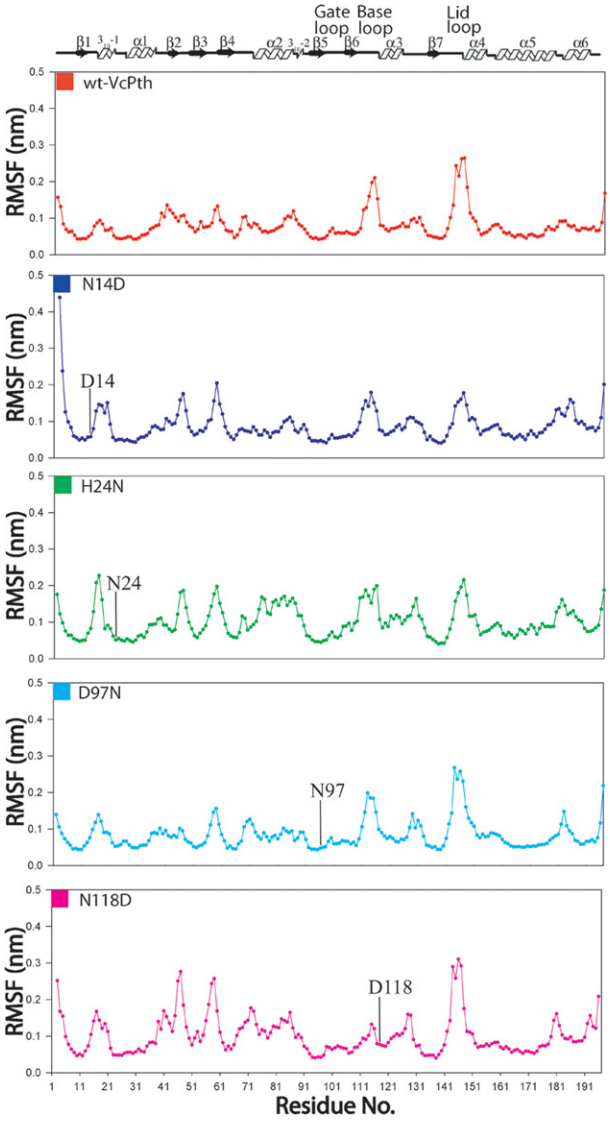

FIGURE 6. Backbone flexibility in terms of RMSF plots for wt-VcPth, N14D, H24N, D97N, and N118D mutants using 10 ns MD simulation study. The RMSF plot is generated using the trajectories during 2–10 ns. Starting trajectories are omitted due to system instability during the first 2 ns. The mutational sites are shown by arrow with appropriate labeling of mutated residues. Crystal structure of the corresponding protein was taken as the starting structure for the corresponding simulation study.

Thermal stabilities of wt-VcPth and its mutants

An overlay of DSC thermograms for wt-VcPth and its mutants is depicted in Figure 7. Wt-VcPth and the mutants show an irreversible two-state thermal unfolding pathway. The thermal stability of wt-VcPth was found to be higher than that of N14D and H24N mutants. The D97N mutation led to a large decrease in the stability of the protein. On the other hand, the N118D mutation was found to increase the stability of the protein. The N72D mutation did not affect the stability. The melting temperatures (T_m) for wt-VcPth, N14D, H24N, N72D, D97N, and N118D were found to be 52.08°C, 46.18°C, 48.62°C, 52.06°C, 42.93°C, and 55.56°C, respectively. Crystal structure and NMR chemical shift perturbation studies show that there is no large global change in the structures of the various mutants of wt-VcPth. However, the importance of the subtle local changes in the hydrogen bonding network because of various mutations,

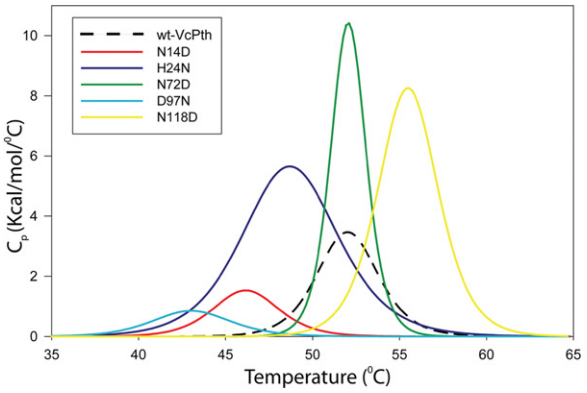

FIGURE 7. Comparison of thermal stability of wt-VcPth with its various mutants: overlay of DSC thermograms for wt-VcPth (black dashed line), N14D (red), H24N (blue), N72D (green), D97N (cyan), and N118D (yellow) mutants. The melting temperatures (T_m) for wt-VcPth, N14D, H24N, N72D, D97N, and N118D mutants were found to be 52.08°C, 46.18°C, 48.62°C, 52.06°C, 42.93°C, and 55.56°C, respectively.

as discussed below, is highlighted through the changes in the stabilities, as reflected from the T_m of various mutants.

It is interesting to mention that the thermal stability changes were qualitatively in the direction of the ΔG changes (ΔG) predicted by the i-Mutant 2.0 server (Capriotti et al. 2005) for the wt-VcPth and its mutants, when the crystal structures were used as the input.

pH titration of wt-VcPth

For wt-VcPth, ^{1}H-^{15}N HSQC experiments were recorded at a pH varying from 7.0 to 5.0, and to map the pH induced CSPs, backbone assignments were carried out by performing standard 2D and 3D experiments on ^{13}C, ^{15}N-labeled wt-VcPth, at pH 5.2. Assignments could be made for all the residues that were assigned at pH 6.5. Interestingly, N118 could again be assigned at pH 5.2, which reflects the pH induced change in the dynamics of N118. Detailed CSP assessment, based on the backbone assignment at pH 5.2, is presented in Supplemental Figure S6. The CSPs reveal that pH mainly affects the catalytic site (H24-N25) and lid regions (H142, H145, D147-V149, G151, and L154). In addition, several regions that are proximal to or interacting with the various titratable histidine residues, like helix α1 (I37-H38); gate loop region (D97 and D100); β6 (F108); and α3–β7 loop (N129) show significant perturbations.

DISCUSSION

The mechanistic understanding of Pth enzyme action has been related to the plasticity of the base loop, gate loop, and lid loop, derived from the comparison of crystal structures of various Pth proteins, and as per this hypothesis, the gate and lid distances are inversely correlated (Selvaraj et al. 2007). The gate and lid distances for wt-VcPth and various mutants are shown in Supplemental Table S6. As can be seen from these values, an inverse correlation between gate and lid distances is not observed. Therefore, this hypothesis will not be discussed further and the focus would be on discussing the stereochemical and dynamic aspects of the catalytic site.

Our work provides a finer insight into the side-chain conformations and dynamics of important catalytic residues and networks of interactions between them, in the unbound state of bacterial Pths. This insight can also aid in the design of inhibitors against bacterial Pth proteins, which are important antimicrobial targets. In our approach, we have carried out an extensive analysis of structure, dynamics, and stability of wt-VcPth and mutants of its most important residues for catalysis, rather than deriving the information by overlaying the crystal structures from different species. Further, since the crystal structure provides only local effects, the long-range effects have been characterized by mapping the magnitude of CSPs. For the aspects dealing with side-chain orientations, we have compared the X-ray crystal structure of the wild-type protein with the crystal structures of the mutants. For global and local time-averaged dynamics, NMR assignments, and dynamics of the wild-type protein have been compared with those of the mutants. On one hand, this approach increases consistency, while on the other hand it minimizes cross-interpretations from two complementary techniques. Therefore, the differences in solvent conditions between the NMR and X-ray studies are not expected to alter the conclusions derived below on the basis of these studies.

We will now discuss the conformations of the side chains of important catalytic residues observed in the crystal structures of various mutants. The distance and orientation information is correlated to the backbone amide dynamics and CSPs obtained through NMR spectroscopy, in order to visualize a time-averaged local electrostatic effect, which is also indicated by the differences observed in the thermal stabilities.

Side-chain orientations of catalytic histidine H24, D97, N118, and N14

Earlier studies have indicated that substrate binding and catalysis both depend on the orientation and dynamics of residues corresponding to N14, H24, D97, and N118 of VcPth (Schmitt et al. 1997; Goodall et al. 2004; Giorgi et al. 2011b; Ito et al. 2012; Singh et al. 2014b). Out of these, the residue corresponding to N14 has specifically been implicated for substrate discrimination (Giorgi et al. 2011b). The H24 residue is involved in three pronged interactions with the side chains of D97, N14, and N118. This interaction is shown in Figure 8 for various mutants.

In the wt-VcPth crystal structure, the orientation of the N118 side chain is defined by the torsion angles χ1 and χ2,

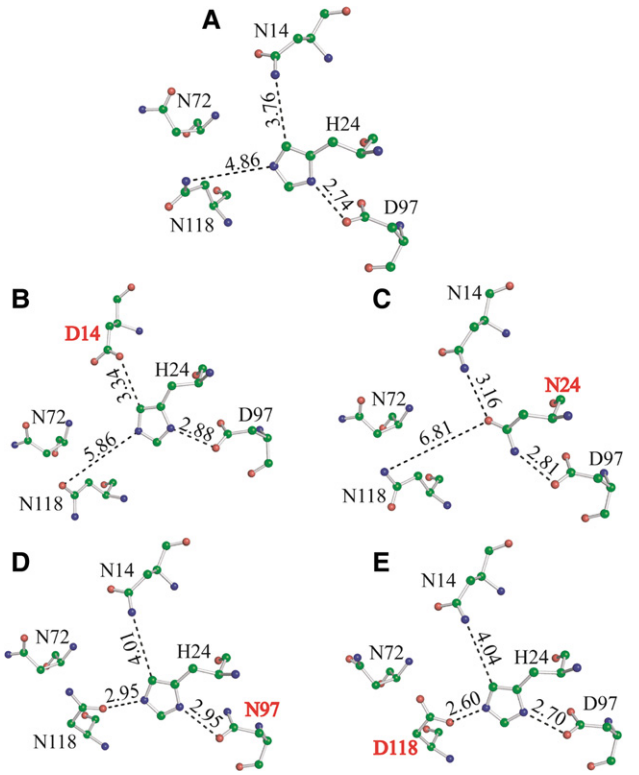

FIGURE 8. Side-chain orientations of catalytic histidine H24, D97, N118, N14, and N72 in (*A*) wt-VcPth, (*B*) N14D, (*C*) H24N, (*D*) D97N, and (*E*) N118D mutants. The minimum interatomic distances (Å) between H24-N14, H24-N118, and H24-D97 are shown as black dashes and labeled.

with χ1 being equal to −70° and χ2 being equal to −40°. In various mutants, the χ1 or χ2 values change to have closer interaction with H24, as shown in Supplemental Table S7. The N14 and N118 distances of closest approach to H24 show important changes in various mutants. The closest distance between the polar groups of N118 and H24 for wt-VcPth is ND2-NE2 = 4.86 Å, while this distance shortens to within hydrogen bonding distance in the D97N and N118D mutants, as shown in Supplemental Table S8. The N14-H24 distance for wt-VcPth is 3.76 Å, and it also shortens to hydrogen bonding distance in the N14D and H24N mutants. The H24 ring is held in place by formation of a salt bridge with D97 and by hydrophobic interactions with V153 and M71. However, competing lateral movements along two orthogonal directions are possible, leading to transient interactions with N14 and N118, as shown by brown dashes in Figure 2. Moreover, formation of a hydrogen bond with N14 could also involve a flipping of the imidazole ring of H24, especially in the case of N14D and D97N mutants, and such flipping of aromatic rings is in the slow time scale regime of NMR dynamics (Ash et al. 2000). Based on the various orientations of these side chains, we propose that in solution, the orientations of these side chains fluctuate dynamically, and they assert a directional time-averaged electrostatic effect. From the distances of closest approach, these electrostatic effects can be correlated to formation of salt bridges/hydrogen bonds between H24 and D97/N118/N14 with the strength D97 > N118 > N14. Further, while the D97-H24 hydrogen bond promotes the nucleophilicity of H24, the N118-H24 and N14-H24 hydrogen bonds may actually decrease the nucleophilicity of H24. Based on the various Pth-substrate docking models, it is reasonable to expect that this decrease would be offset by the positioning of the penultimate amide bond and the scissile ester bond of the peptidyl-tRNA substrate, leading to substrate selectivity and hydrolysis, as shown in Figure 2.

Dynamics of N118

Various biochemical and structural studies have indicated that the highly conserved asparagine residue corresponding to N118 of VcPth could play a very important role in catalysis by binding to the carbonyl moiety of the scissile ester group (Fromant et al. 1999; Ito et al. 2012). It has been suggested that N118 could also be involved in positioning of the water molecule involved in initiating the hydrolysis reaction. Therefore, it is important to characterize the interactions and dynamics of this residue. NMR assignments of mutants reported above hint at the existence of an important interaction between N118 and H24. This is related to the discovery of an interesting motional change involving the amide NH of the N118 residue. In the X-ray crystal structures of most of the bacterial Pth proteins, no direct interaction is observed between the corresponding residues (Schmitt et al. 1997; Clarke et al. 2011; Hughes et al. 2012; Kaushik et al. 2013; Vandavasi et al. 2014). Therefore, this interaction cannot be directly identified and is "hidden" in bacterial Pth proteins. In the VcPth crystal structure also, H24 is hydrogen bonded to D97, but not to N118. In the ^{1}H–^{15}N HSQC spectrum of wt-VcPth, the amide correlation peak corresponding to N118 is not observed at pH 6.5. The peak for asparagine at this particular position is also not observed in the HSQC spectra of MtPth and MsPth at pH 6.5 (Pulavarti et al. 2008; Kabra et al. 2016). The absence of an amide peak from the HSQC spectrum could be because of the fast exchange with the solvent or because of an intermediate rate of fluctuations on the NMR time scale, which could lead to line broadening. The dynamics of the N118 amide NH vector are highly sensitive and are influenced by various mutations, as described below. Such dependence strongly favors intermediate time scale exchange over solvent exchange as the reason for the absence of the amide peak of N118 in the HSQC spectrum. Through NMR assignments, the cross peak corresponding to the amide of residue N118 could be identified in the HSQC spectrum of H24N, N72D, and N118D mutants. The expanded regions of HSQC showing the NH peak of residue N118, and the strips from HNCACB experiments depicting the sequential assignments

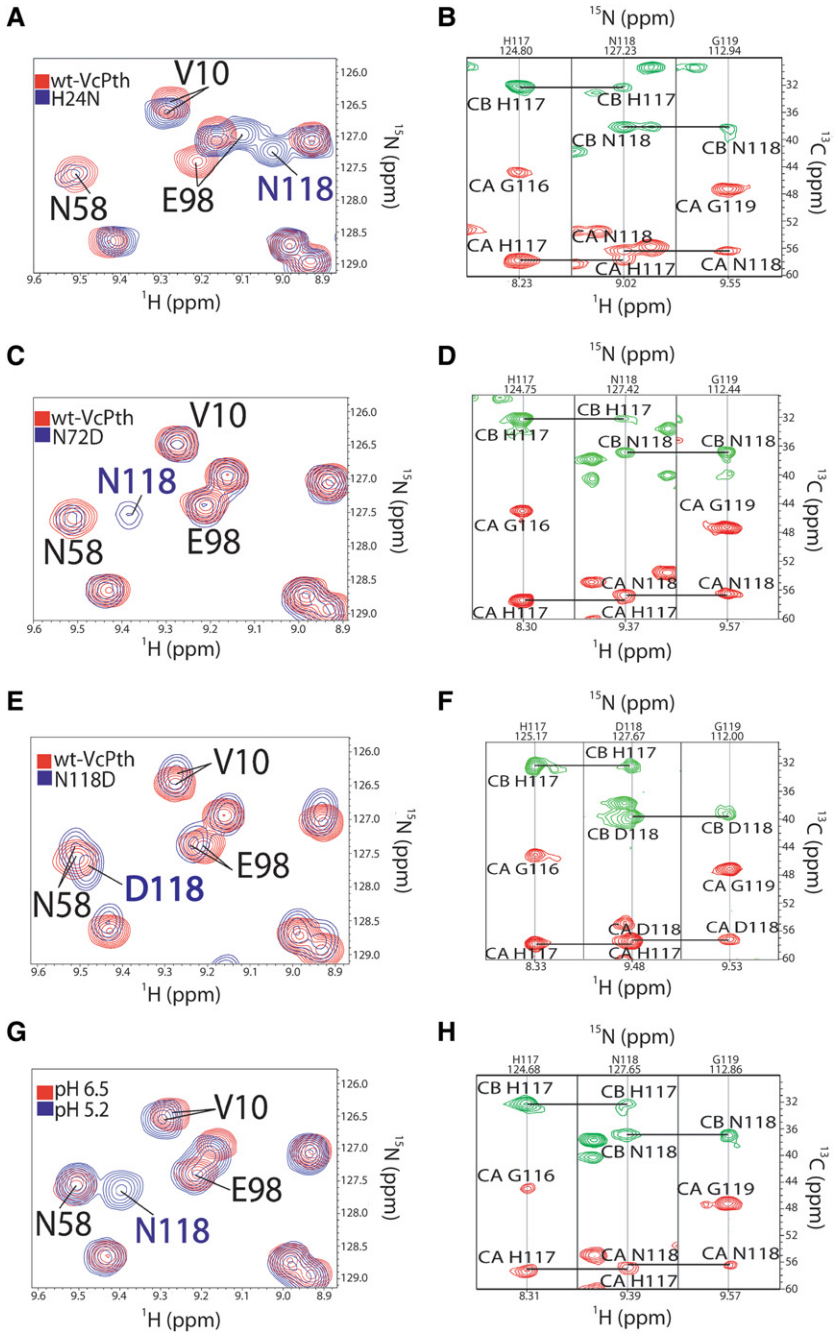

FIGURE 9. Hidden interaction between H24 and N118: (*A*), (*C*), (*E*), and (*G*) Overlapped ^{1}H–^{15}N HSQC spectra of N118 assignment region for wt-VcPth at pH 6.5 with the H24N mutant, with the N72D mutant, with the N118D mutant, and wt-VcPth at pH 5.2, respectively. (*B*), (*D*), (*F*), and (*H*) Strips corresponding to segment H117-G119 depicting the sequential connectivity of N118, from the 3D HNCACB experiment for H24N mutant, N72D mutant, N118D mutant, and wt-VcPth at pH 5.2, respectively.

for the H117-G119 segment for various mutants, are shown in Figure 9. We interpret that the H24N mutation results in enhancement of N118 amide NH vector dynamics from intermediate to fast chemical exchange, while the N72D and N118D mutations change the dynamics from intermediate to slow exchange (Fig. 9). The possible side-chain conformations for the residue corresponding to N118, with respect to the side chain of the catalytic histidine, are shown in Figure 10. The backbone amide NH of residue N118 is hydrogen bonded to the carbonyl moiety of its own side chain, while its side-chain group strongly binds to H24 in one out of the three conformations shown. Therefore, the disappearance and appearance of the amide peak of residue N118 is related to the time-averaged binding of its amide group to H24, which possibly affects the wobble frequency of the helix α3, of which N118 is the N-cap residue. This wobbling motion of helix α3 and the movement of the preceding base loop (G111-H117) may be envisaged to play an important role in the accommodation of the scissile ester group and the peptidyl portion of the substrate.

More evidence of local electrostatics playing a role in the dynamics of N118 is obtained from NMR-based pH titration experiments, as shown in Figure 9G,H. The p*K*a of the catalytic histidine has been reported to be 6.3 for *E. coli* Pth (Goodall et al. 2004). At lower pH, the NE2 of H24 gets protonated. It can be anticipated that this would lead to changes in its interactions with the side chain of N118. Strikingly, upon lowering of the pH from 6.5 to 6.0, the amide correlation peak for N118 becomes visible in the ^{1}H-^{15}N HSQC spectrum of VcPth. In addition to N118, the change in pH majorly affects the lid residues of VcPth. In the context of local electrostatics, it is also important to consider that N14D mutation does not lead to the appearance of a N118 peak in the HSQC spectrum.

In conclusion, by characterizing the structure, dynamics, and stabilities of wt-VcPth and its mutants, the important role of the N14/N118-H24-D97 interaction network has been highlighted for both catalysis and substrate selectivity. H24-D97 interaction is most important for catalysis. In the four mutants studied, along with the changes in orientation, there are also distance changes that show the possibility of formation of competing orthogonal and transient N14-H24 and N118-H24 hydrogen bonds, which may involve

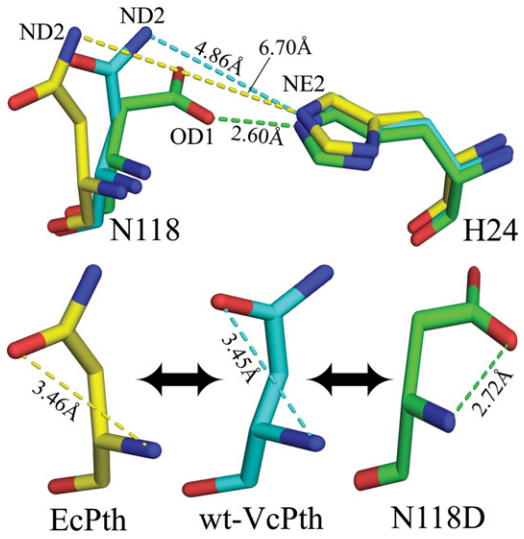

FIGURE 10. Relative side-chain orientations between the catalytic histidine and N-cap residue of helix α3 for wt-VcPth (cyan), N118D mutant (green), and EcPth (yellow). (*Top*) The minimum distances between the side-chain amide of the N-cap residue and side chain of catalytic histidine are indicated. (*Bottom*) The minimum distance between the main chain amide NH and side-chain amide/carboxylate are indicated for the N-cap residue of helix α3 for wt-VcPth (cyan), N118D mutant (green), and EcPth (yellow). Double-sided arrows represent possible interconversions between these conformations in solution.

flipping of the histidine imidazole ring. H24N, N72D, and N118D mutations and lowering of pH below the p*K*a of the catalytic histidine residue lead to changes in dynamics of the amide NH vector of N118, which reflect the changes in local electrostatic effects and hydrogen bonding networks between these residues. While most of the tRNA portion of the substrate can be expected to be rigid, the CCA-arm and the peptidyl region are likely to be comparatively more flexible (Alexander et al. 2010). We propose that the slow wobble of the helix α3 and the movements of the proximal peptide binding regions may act as a flypaper to bind and position the scissile ester group and the peptide portion of the substrate, with further selection for hydrolysis depending on the N14-H24 interactions. It may be predicted that any potent inhibitor of Pth would require simultaneous interactions with N14 and N118 to lock the protein into an inactive conformation. Overall, our approach of exhaustive characterization using mutagenesis in combination with X-ray crystal structures, NMR structure and assignments, MD simulations, and DSC measurements has provided, on the basis of internal consistency of results, significantly improved understanding of the hydrogen bonding networks and related dynamics operating in the structural segments important for the catalysis. These interactions are important to unravel not only a mechanistic understanding of enzyme action but also for design and testing of inhibitors against this protein. NMR assignments of the various mutants made by us will be very useful for this purpose.

MATERIALS AND METHODS

Cloning, overexpression, and purification

The open reading frame of Pth was PCR (polymerase chain reaction) amplified from the genomic DNA of *Vibrio cholerae* (El Tor strain) using 5′-CATGCCATGGTGAGTCAGCC-TATCAAAC TCCTT-3′ and 5′-CCCAAGCTTCTATGCACTGGCCTTAAAAGC GTG-3′ as forward and reverse primers, respectively. These primers were designed to contain NcoI and HindIII restriction enzyme sites for forward and reverse primers, respectively. The PCR amplified product was digested with NcoI and HindIII, and ligated into pET-NH6 vector previously digested with the same enzymes. The clone was confirmed using DNA sequencing. N14D, H24N, N72D, D97N, and N118D mutants were created for mutational analysis and verified using DNA sequencing. All clones were transformed into the BL21 (λDE3) strain of *E. coli*. The recombinant proteins were purified by two-step purification using Ni-NTA metal affinity chromatography followed by Superdex G-75 gel filtration chromatography. A single sharp peak corresponding to 22 kDa was observed in the chromatogram of each protein, which reflects monomeric form for wt-VcPth and its mutants in solution. The 260/280 ratio for the FPLC purified protein was found to be ~0.7, which shows that the protein was >95% pure and nucleotide contamination was removed. Purity of the protein samples was checked by 15% SDS-PAGE and protein estimation was done using standard Bradford assay.

NMR spectra acquisition, data processing, and structure calculation

^{15}N and $^{15}N/^{13}C$ labeled proteins were purified as described above. Purified proteins were extensively dialyzed and further concentrated using an Amicon centricon membrane with a 3 kDa cutoff. The final NMR samples were prepared in 20 mM NaH_2PO_4 (pH 6.5), 50 mM NaCl, 1 mM DTT and 0.1% NaN_3 (w/v), in either $H_2O/^2H_2O$ (19:1, v/v) or 100% ^2H_2O, for acquisition of NMR spectra. All the backbone and most of the side-chain assignment experiments were recorded at 298 K on a Varian Inova 600 MHz spectrometer, while the HCCH-TOCSY, CBHD, CBHE, aromatic ^{13}C-HSQC, and 3D-NOESY-HSQC experiments were recorded at 298 K on a Bruker Avance 800 MHz spectrometer. Both the spectrometers were equipped with pulse field gradients triple resonance cryoprobe with actively shielded Z gradients. The proton chemical shifts were referenced directly with 2, 2-dimethyl-2-silapentanesulfonic acid (DSS) as an external calibration agent, whereas the ^{15}N and ^{13}C chemical shifts were referenced indirectly. All the spectra were processed with NMRPipe (Delaglio et al. 1995) and analyzed using CARA (Keller 2004).

Chemical shift assignments of HN, N, CO, CA, and CB resonances were performed manually using five triple resonance experiments, HNCO, HN(CA)CO, HNCA, HNCACB, and CBCA(CO)NH. The remainders of the chemical shift assignments were also obtained manually using a combination of several spectra including H(CCO)NH-TOCSY, (H)C(CO)NH-TOCSY, HCCH-TOCSY, CBHD, CBHE, and aromatic ^{13}C-HSQC. Distance restraints were derived from the analysis of the 3D ^{15}N-edited NOESY-HSQC spectra (100 msec), ^{13}C-edited (aliphatic) NOESY-HSQC (150 msec), and ^{13}C (aromatic)-edited NOESY-HSQC (150 msec) spectra.

The upper distance limits for structure calculations were derived from cross-peak volumes that were calibrated using the CALIBA peak calibration routine in CYANA-3.0 (Guntert et al. 1991, 1997). The torsion angle constraints were obtained from assigned backbone chemical shifts using the program TALOS+ (Shen et al. 2009). Hydrogen bond restraints were introduced into the regions where amide protons were protected from ^2H_2O exchange and where there were regular secondary structural elements based on characteristic NOEs. For each hydrogen bond restraint, upper limits of 2.0 Å and 3.0 Å were used for the distances from amide proton to acceptor atom and amide nitrogen atom to acceptor atom, respectively. The structural calculations were performed with program CYANA-3.0. A total of 500 randomized conformers were generated and 10 conformers with lowest target function were selected. The final structure was refined using CNS with explicit water as the solvent (Brünger et al. 1998; Linge et al. 2003). The program PROCHECK-NMR was used to analyze the quality of the structures (Laskowski et al. 1993, 1996). The programs PyMOL, MOLMOL, and Chimera were used for generating figures for structures.

Relaxation measurements

All relaxation experiments were recorded on uniformly ^{15}N-labeled 0.5 mM wt-VcPth, H24N mutant, and N118D mutant, at 298 K on an Agilent-DD2 700 MHz spectrometer equipped with a PFG triple nuclear cryoprobe. R_1 and R_2 relaxation rates were measured from spectra with different relaxation delays: 0, 10, 70, 110×2, 280, 450, 610×2, 890, and 1330 msec for R_1 and 10, 30×2, 50, 70, 90×2, 110 and 130 msec for R_2. The relaxation rates for both R_1 and R_2 were determined from the decay of the intensity of each ^{1}H–^{15}N crosspeak in this series of spectra. The R_1 and R_2 values were obtained by using the program Curvefit. The errors in individual R_1 and R_2 measurements were estimated by Monte Carlo simulations. The R_2 values were trimmed by 15% to account for inhomogeneities. The steady-state heteronuclear $\{^1$H$\}$-^{15}N NOE values were obtained by recording spectra with and without a proton presaturation period (3 sec) applied before the start of the ^{1}H-^{15}N HSQC experiment (Farrow et al. 1994). The relaxation delay of 3 sec was used between FIDs in the steady-state heteronuclear $\{^1$H$\}$-^{15}N NOE experiment.

Model-free analysis

The heteronuclear ^{15}N relaxation parameters R_1 and R_2, and the steady-state ($\{^1$H$\}$-^{15}N NOE) values were analyzed by model-free formalism as proposed by Lipari and Szabo et al. (1982a,b) and further extended by Clore et al. (1990). In this approach, the overall and internal molecular motions are assumed to be independent. Motional parameters were determined using the program FAST-Modelfree (Roger and Loria 2003) interfaced with Modelfree 4.1 (Palmer et al. 1991). The statistical criteria used for model description were as described in Mandel et al. (1995). For model-free analysis, the N–H bond length was assumed to be 1.02 Å, and a ^{15}N chemical shift anisotropy value of 170 ppm was considered. The uncertainties in R_1 and R_2 were set to an upper limit of 3.5% and 6%, respectively. While the uncertainties in steady state $\{^1$H$\}$-^{15}N NOE were fixed at 0.05. In FAST-Modelfree, SSE (sum square error) Cutoff and *F*-test Cutoff for isotropic diffusion tensors were set to 0.95 and 0.80, respectively, for the comparison of Lipari–Szabo models. The quality of fit between the experimental data and the theoretical model was assessed by comparing the optimal value of SSE with the $\alpha = 0.05$ critical value of the distribution SSE determined from the Monte Carlo simulations. The critical value is the value of SSE that is exceeded by the specified fraction of simulated data.

Crystallization, data collection, and structure determination

For crystallization trials, protein was concentrated to varied concentrations using a 3 kDa cutoff centricon. Preliminary crystallization trials were performed using the hanging drop vapor diffusion method. The best crystallization conditions for wt-VcPth were determined to exist when 2 µL of 12 mg/mL VcPth was mixed with 2 µL of reservoir solution of 20% (w/v) PEG-4000 and 200 mM ammonium acetate in 100 mM sodium citrate buffer (pH 8.0). Using these conditions, suitable crystals for X-ray diffraction could be grown in 1 wk at 296 K. Prior to data collection, crystals were soaked in reservoir solution containing 25% (w/v) PEG-4000 as a cryoprotectant. The native crystal was mounted onto an appropriate-sized nylon loop, flash-cooled, and stored in liquid nitrogen. The data were collected with Rigaku FR-E+ SuperBright with a wavelength $\lambda = 1.54$ Å using the R-AXIS IV++ detector. A complete data set (360°, 0.5° oscillation diffraction images) was collected and resulting images were indexed and integrated using the HKL-2000. Initial phases were obtained by the molecular replacement method with the program MOLREP (Vagin and Teplyakov 1997), using the structure of *Salmonella typhimurium* Pth (PDB accession code 4P7B) as a search model. The same procedure was followed for the crystallization of N14D, H24N, D97N, and N118D mutants.

MD simulations

MD simulations for the wt-VcPth and its four active site mutants (N14D, H24N, D97N, and N118D) were carried out using the crystal structures with the GROMACS code (version 4.5.6) and Gromos43a1 force field for 10 nanoseconds (nsec). The system was prepared using the protein crystal structures and all the water molecules of the crystal structures were removed. Missing residues in the crystal structures were added using NOC software. GROMACS utilities for system preparation were used thoroughly. The system was then solvated using a cubic SPC water box followed by the charge neutralization of the system. Subsequently the entire system was minimized using the steepest descent algorithm. The system was then equilibrated for 100 picoseconds (psec) at 300 K using an NVT ensemble and for 100 psec using an NPT ensemble. Production MD simulation was run for 10 ns. After the simulation, various properties like total energy, rmsd, radius of gyration, and residue wise rmsf (root mean square fluctuation) profiles were computed and analyzed.

Thermal denaturation study

T_m values of wt-VcPth and mutants (N14D, H24N, N72D, D97N, and N118D) were measured in the NMR buffer conditions using a high precision Microcal VP-DSC calorimeter from GE Healthcare Life sciences. All samples were filtered, degassed, and loaded into the cells, avoiding bubble formation. The baseline of

the instrument was recorded before the experiments with both cells filled with buffer. The volume of reference and sample cells was 0.51 mL. All proteins were extensively dialyzed against phosphate buffer (20 mM phosphate buffer, pH 6.5, containing 50 mM NaCl, 1 mM DTT, and 0.1% sodium azide) and brought to a concentration of 0.01 mM. The protein samples and buffer solutions were thoroughly degassed for 20 min just before the experiment. DSC scans were performed from 20 to 65°C at a heating rate of 60°C per hour. Buffer scans were subtracted from the sample scans, and the data were normalized with respect to protein concentration, scan rate, and electrical calibration of the calorimeter, to generate the excess heat capacity vs. temperature thermogram of the sample. The baselines before and after transition were selected for the thermogram with the Origin 7.0 program, and the transition enthalpy, and T_m were determined by integration and nonlinear curve fitting to a two-state model.

DATA DEPOSITION

NMR chemical shift assignment for wt-VcPth, N14D, H24N, N72D, and N118D mutants have been deposited at BMRB with accession codes 19731, 26876, 26875, 26877, and 26878, respectively. The atomic coordinates of wt-VcPth solution structure, wt-VcPth crystal structure with bound citrate, wt-VcPth crystal structure without citrate, N14D, H24N, D97N, and N118D mutant crystal structures have been deposited in the protein data bank with accession codes 2MJL, 4ZXP, 5VGZ, 5IMB, 5B6J, 5IKE, and 4Z86, respectively.

SUPPLEMENTAL MATERIAL

Supplemental Material is available for this article.

ACKNOWLEDGMENTS

We are grateful to the Sophisticated Analytical Instrument Facility (SAIF) of CSIR-CDRI, Lucknow, the National facility for high-field NMR at TIFR, Mumbai, India and CBMR, Lucknow for access to the Varian 700 MHz and Bruker 800 MHz spectrometers, respectively. We also thank the X-ray diffraction facility of the National Institute of Immunology (NII), New Delhi, India, for X-ray data collection. This work was supported by grants from Council of Scientific and Industrial Research (CSIR) Network Projects BSC0113 and BSC0104, and Department of Biotechnology (DBT), New Delhi, India. A.K. and S.S. are recipients of research fellowships from the Indian Council of Medical Research (ICMR) and the University Grants Commission (UGC), New Delhi, India. S.V.S.R. K.P. and R.Y. were recipients of research fellowships from CSIR and DBT, New Delhi, India. S.S. is grateful to AcSIR (Academy of Scientific and Innovative Research) for PhD registration. This is communication number 9373 from CSIR-CDRI.

Received May 24, 2016; accepted November 7, 2016.

REFERENCES

Alexander RW, Eargle J, Schulten ZL. 2010. Experimental and computational determination of tRNA dynamics. *FEBS Lett* **584:** 376–386.

Ash EL, Sudmeier JL, Day RM, Vincent M, Torchilin EV, Haddad KC, Bradshaw EM, Sanford DG, Bachovchin WW. 2000. Unusual 1H NMR chemical shifts support (His) $C^{\varepsilon 1}$···O==C H-bond: proposal for reaction-driven ring flip mechanism in serine protease catalysis. *Proc Natl Acad Sci* **97:** 10371–10376.

Atherly AG. 1978. Peptidyl-transfer RNA hydrolase prevents inhibition of protein synthesis initiation. *Nature* **275:** 769.

Bal NC, Agrawal H, Meher AK, Arora A. 2007. Characterization of peptidyl-tRNA hydrolase encoded by open reading frame Rv1014c of *Mycobacterium tuberculosis* H37Rv. *Biol Chem* **388:** 467–479.

Blake-Hall J, Walker O, Fushman D. 2004. Characterization of the overall rotational diffusion of a protein from ^{15}N relaxation measurements and hydrodynamic calculations. *Methods Mol Biol* **278:** 139–160.

Bonin PD, Choi GH, Trepod CM, Mott JE, Lyle SB, Cialdella JI, Sarver RW, Marshall VP, Erickson LA. 2002. Expression, purification, and characterization of peptidyl-tRNA hydrolase from *Staphylococcus aureus*. *Protein Expr Purif* **24:** 123–130.

Brünger AT, Adams PD, Clore GM, DeLano WL, Gros P, Grosse-Kunstleve RW, Jiang JS, Kuszewski J, Nilges M, Pannu NS, et al. 1998. Crystallography and NMR system: a new software suite for macromolecular structure determination. *Acta Crystallogr D Biol Crystallogr* **54:** 905–921.

Caplan AB, Menninger JR. 1979. Tests of the ribosomal editing hypothesis: amino acid starvation differentially enhances the dissociation of peptidyl-tRNA from the ribosome. *J Mol Biol* **134:** 621–637.

Capriotti E, Fariselli P, Casadio R. 2005. I-Mutant2.0: predicting stability changes upon mutation from the protein sequence or structure. *Nucleic Acids Res* **33:** W306–W310.

Clarke TE, Romanov V, Lam R, Gothe SA, Peddi SR, Razumova EB, Lipman RSA, Branstrom AA, Chirgadze NY. 2011. Structure of *Francisella tularensis* peptidyl-tRNA hydrolase. *Acta Crystallogr Sect F Struct Biol Cryst Commun* **67:** 446–449.

Clore GM, Szabo A, Bax A, Kay LE, Driscoll PC, Gronenborn AM. 1990. Deviations from the simple two-parameter model free approach to the interpretation of nitrogen-15 nuclear magnetic relaxation of proteins. *J Am Chem Soc* **112:** 4989–4991.

Cruz-vera LR, Toledo I, Hernandez-Sanchez J, Guarneros G. 2000. Molecular basis for the temperature sensitivity of *Escherichia coli pth*(Ts). *J Bacteriol* **182:** 1523–1528.

Cruz-Vera LR, Magos-Castro MA, Zamora-Romo E, Guarneros G. 2004. Ribosome stalling and peptidyl-tRNA drop-off during translational delay at AGA codons. *Nucleic Acids Res* **32:** 4462–4468.

Das G, Varshney U. 2006. Peptidyl-tRNA hydrolase and its critical role in protein biosynthesis. *Microbiology* **152:** 2191–2195.

Delaglio F, Grzesiek S, Vuister GW, Zhu G, Pfeifer J, Bax A. 1995. NMRPipe: a multidimensional spectral processing system based on UNIX pipes. *J Biomol NMR* **6:** 277–293.

Farrow NA, Muhandiram R, Singer AU, Pascal SM, Kay CM, Gish G, Shoelson SE, Pawson T, Forman-Kay JD, Kay LE. 1994. Backbone dynamics of a free and phosphopeptide-complexed Src homology 2 domain studied by 15N NMR relaxation. *Biochemistry* **33:** 5984–6003.

Fromant M, Plateau P, Schmitt E, Mechulam Y, Blanquet S. 1999. Receptor site for the 5′-phosphate of elongator tRNAs governs substrate selection by peptidyl-tRNA hydrolase. *Biochemistry* **38:** 4982–4987.

Giorgi L, Bontems F, Fromant M, Aubard C, Blanquet S, Plateau P. 2011a. The RNA binding site of *Escherichia coli* peptidyl-tRNA hydrolase. *J Biol Chem.* **286:** 39585–39594.

Giorgi L, Plateau P, O'Mahony G, Aubard C, Fromant M, Thureau A, Grøtli M, Blanquet S, Bontems F. 2011b. NMR-based substrate analog docking to *Escherichia coli* peptidyl-tRNA hydrolase. *J Mol Biol* **412:** 619–633.

Goodall JJ, Chen GJ, Page MG. 2004. Essential role of histidine 20 in the catalytic mechanism of *Escherichia coli* peptidyl-tRNA hydrolase. *Biochemistry* **43:** 4583–4591.

Guntert P, Qian YQ, Otting G, Muller M, Gehring W, Wuthrich K. 1991. Structure determination of the *Antp*(C39→S) homeodomain from nuclear magnetic resonance data in solution using a novel strategy for the structure calculation with the programs DIANA, CALIBA, HABAS and GLOMSA. *J Mol Biol* **217:** 531–540.

Guntert P, Mumenthaler C, Wuthrich K. 1997. Torsion angle dynamics for NMR structure calculation with the new program DYANA. *J Mol Biol* **273:** 283–298.

Hames MC, McFeeters H, Holloway WB, Stanley CB, Urban VS, McFeeters RL. 2013. Small molecule binding, docking, and characterization of the interaction between Pth1 and peptidyl-tRNA. *Int J Mol Sci* **14:** 22741–22752.

Heurgue-Hamard V, Karimi R, Mora L, MacDougall J, Leboeuf C, Grentzmann G, Ehrenberg M, Buckingham RH. 1998. Ribosome release factor RF4 and termination factor RF3 are involved in dissociation of peptidyl-tRNA from the ribosome. *EMBO J* **17:** 808–816.

Hughes RC, McFeeters H, Coates L, McFeeters RL. 2012. Recombinant production, crystallization and X-ray crystallographic structure determination of the peptidyl-tRNA hydrolase of *Pseudomonas aeruginosa*. *Acta Crystallogr Sect F Struct Biol Cryst Commun* **68:** 1472–1476.

Ito K, Murakami R, Mochizuki M, Qi H, Shimizu Y, Miura K, Udea T, Uchiumi T. 2012. Structural basis for the substrate recognition and catalysis of peptidyl-tRNA hydrolase. *Nucleic Acids Res* **40:** 10521–10531.

Kabra A, Fatma F, Shahid S, Pathak PP, Yadav R, Pulavarti SV, Tripathi S, Jain A, Arora A. 2016. Structural characterization of peptidyl-tRNA hydrolase from *Mycobacterium smegmatis* by NMR spectroscopy. *Biochim Biophys Acta* **1864:** 1304–1314.

Karimi R, Pavlov MY, Heurgue-Hamard V, Buckingham RH, Ehrenberg M. 1998. Initiation factors IF1 and IF2 synergistically remove peptidyl-tRNAs with short polypeptides from the P-site of translating *Escherichia coli* ribosomes. *J Mol Biol* **281:** 241–252.

Kaushik S, Singh N, Yamini S, Singh A, Sinha M, Arora A, Kaur P, Sharma S, Singh TP. 2013. The mode of inhibitor binding to peptidyl-tRNA hydrolase: binding studies and structure determination of unbound and bound peptidyl-tRNA hydrolase from *Acinetobacter baumannii*. *PLoS One* **8:** e67547.

Keller R. 2004. "Optimizing the process of nuclear magnetic resonance spectrum analysis and computer aided resonance assignment." PhD thesis, Swiss Federal Institute of Technology, Zurich, Switzerland.

Kumar A, Singh N, Yadav R, Kumar RP, Sharma S, Arora A, Singh TP. 2012. Crystal structure of peptidyl-tRNA hydrolase from *Mycobacterium smegmatis* reveals novel features related to enzyme dynamics. *Int J Biochem Mol Biol* **23:** 58–69.

Laskowski RA, MacArthur MW, Moss DS, Thornton JM. 1993. PROCHECK: a program to check the stereochemical quality of protein structures. *J Appl Crystallogr* **26:** 283–291.

Laskowski RA, Rullmannn JA, MacArthur MW, Kaptein R, Thornton JM. 1996. AQUA and PROCHECK-NMR: programs for checking the quality of protein structures solved by NMR. *J Biomol NMR* **8:** 477–486.

Liang B, Arora A, Tamm LK. 2010. Fast-time scale dynamics of outer membrane protein A by extended model-free analysis of NMR relaxation data. *Biochim Biophys Acta* **1798:** 68–76.

Linge JP, Williams MA, Spronk CA, Bonvin AM, Nilges M. 2003. Refinement of protein structures in explicit solvent. *Proteins* **50:** 496–506.

Lipari G, Szabo A. 1982a. Model-free approach to the interpretation of nuclear magnetic resonance relaxation in macromolecules. 1. Theory and range of validity. *J Am Chem Soc* **104:** 4546–4559.

Lipari G, Szabo A. 1982b. Model-free approach to the interpretation of nuclear magnetic resonance relaxation in macromolecules. 2. Analysis of experimental results. *J Am Chem Soc* **104:** 4559–4570.

Mandel AM, Akke M, Palmer AG. 1995. Backbone dynamics of *Escherichia coli* ribonuclease HI: correlations with structure and function in an active enzyme. *J Mol Biol* **246:** 144–163.

Menez J, Buckingham RH, de Zamaroczy M, Campelli CK. 2002. Peptidyl-tRNA hydrolase in *Bacillus subtilis*, encoded by spoVC, is essential to vegetative growth, whereas the homologous enzyme in *Saccharomyces cerevisiae* is dispensable. *Mol Microbiol* **45:** 123–129.

Menninger JR. 1976. Peptidyl transfer RNA dissociates during protein synthesis from ribosomes of *Escherichia coli*. *J Biol Chem* **251:** 3392–3398.

Menninger JR. 1979. Accumulation of peptidyl-tRNA is lethal to *Escherichia coli*. *J Bacteriol* **137:** 694–696.

Palmer AG, Rance M, Wright PE. 1991. Intramolecular motions of a zinc finger DNA binding domain from Xfin characterized by proton-detected natural abundance 13C heteronuclear NMR-spectroscopy. *J Am Chem Soc* **113:** 4371–4380.

Pulavarti SV, Jain A, Pathak PP, Mahmood A, Arora A. 2008. Solution structure and dynamics of peptidyl-tRNA hydrolase from *Mycobacterium tuberculosis* H37Rv. *J Mol Biol* **378:** 165–177.

Roger C, Loria JP. 2003. FAST-Modelfree: a program for rapid automated analysis of solution NMR spin relaxation data. *J Biomol NMR* **26:** 203–213.

Schmitt E, Mechulam Y, Fromant M, Plateau P, Blanquet S. 1997. Crystal structure at 1.2 Å resolution and active site mapping of *Escherichia coli* peptidyl-tRNA hydrolase. *EMBO J* **16:** 4760–4769.

Selvaraj M, Roy S, Singh NS, Sangeetha R, Varshney U, Vijayan M. 2007. Structural plasticity and enzyme action: crystal structures of *Mycobacterium tuberculosis* peptidyl-tRNA hydrolase. *J Mol Biol* **372:** 186–193.

Shen Y, Delaglio F, Cornilescu G, Bax A. 2009. TALOS+: a hybrid method for predicting protein backbone torsion angles from NMR chemical shifts. *J Biomol NMR* **44:** 213–223.

Singh A, Gautam L, Sinha M, Bhushan A, Kaur P, Sharma S, Singh TP. 2014a. Crystal structure of peptidyl-tRNA hydrolase from a gram-positive bacterium, *Streptococcus pyogenes* at 2.19 Å resolution shows the closed structure of the substrate-binding cleft. *FEBS Open Bio* **4:** 915–922.

Singh A, Kumar A, Gautam L, Sharma P, Sinha M, Bhushan A, Kaur P, Sharma S, Arora A, Singh TP. 2014b. Structural and binding studies of peptidyl-tRNA hydrolase from *Pseudomonas aeruginosa* provide a platform for the structure based inhibitor design against peptidyl-tRNA hydrolase. *Biochem J* **463:** 329–337.

Vagin A, Teplyakov A. 1997. MOLREP: an automated program for molecular replacement. *J Appl Crystallogr* **30:** 1022–1025.

Vandavasi V, Taylor-Creel K, McFeeters RL, Coates L, McFeeters H. 2014. Recombinant production, crystallization and X-ray crystallographic structure determination of peptidyl-tRNA hydrolase from *Salmonella typhimurium*. *Acta Crystallogr F Struct Biol Commun* **70:** 872–877.